RESEARCH ARTICLE | NOVEMBER 29 2022

Nucleation and growth mechanism for atomic layer deposition of Al_2O_3 on two-dimensional WS_2 monolayer

Special Collection: Atomic Layer Deposition (ALD)

Tsu-Ting Lee; Kashi Chiranjeevulu; Sireesha Pedaballi; Daire Cott; Annelies Delabie; Chang-Fu Dee; Edward Yi Chang

Journal of Vacuum Science & Technology A 41, 013201 (2023)
https://doi.org/10.1116/6.0001913

CrossMark

30 June 2023 13:30:10

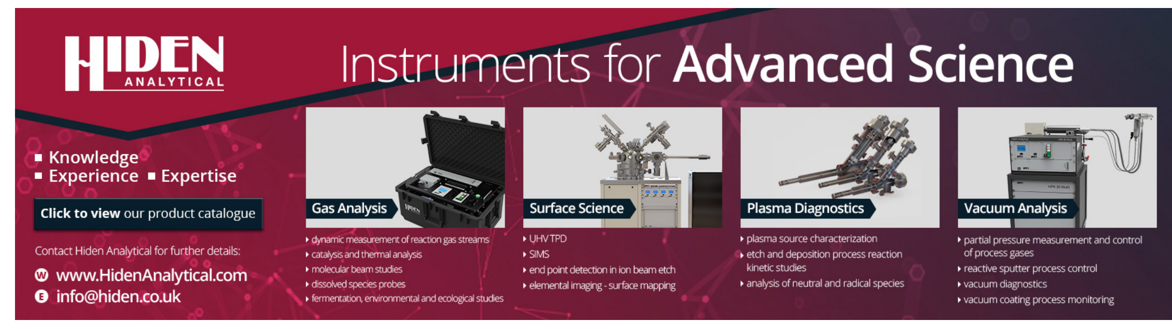

JVST A
Journal of Vacuum Science & Technology A
ARTICLE
avs.scitation.org/journal/jva

Nucleation and growth mechanism for atomic layer deposition of Al_2O_3 on two-dimensional WS_2 monolayer

Cite as: J. Vac. Sci. Technol. A **41**, 013201 (2023); doi: 10.1116/6.0001913
Submitted: 12 April 2022 · Accepted: 18 October 2022 ·
Published Online: 29 November 2022

View Online

Export Citation

CrossMark

Tsu-Ting Lee,[1] Kashi Chiranjeevulu,[1,2] Sireesha Pedaballi,[1,2] Daire Cott,[3] Annelies Delabie,[3] Chang-Fu Dee,[4] and Edward Yi Chang[1,2]

AFFILIATIONS

[1]International College of Semiconductor Technology, National Yang-Ming Chiao Tung University, 1001 University Road, Hsinchu 30010, Taiwan
[2]Department of Materials Science and Engineering, National Yang-Ming Chiao Tung University, 1001 University Road, Hsinchu 30010, Taiwan
[3]Department of Chemistry, KU Leuven (University of Leuven), Belgium, IMEC, 3001 Leuven, Belgium
[4]Institute of Microengineering and Nanoelectronics (IMEN), University of Kebangsaan Malaysia, 43600 Bangi, Selangor, Malaysia

Note: This paper is part of the 2023 Special Topic Collection on Atomic Layer Deposition (ALD).

30 June 2023 13:30:10

ABSTRACT

Nanoelectronics holds significant promise for two-dimensional (2D) semiconducting transition metal dichalcogenide (TMD) applications. On a polycrystalline WS_2 monolayer created by metal-organic chemical vapor deposition (MOCVD) at 950 °C, we studied the nucleation, growth, and development of Al_2O_3 atomic layer deposition (ALD) on a SiO_2/Si substrate. In this investigation, we used various complementary characterization methods, such as Raman spectroscopy, elastic recoil detection, atomic force microscopy, and time-of-flight secondary ion mass spectrometry, to understand thoroughly the intrinsic reactivity of WS_2. Strong peak intensity changes at the interfaces in the Raman line scans of the SiO_2/Si patterns suggest extremely crystalline WS_2. After multiple ALD cycles, triangular WS_2 crystals were decorated to provide a two-dimensional growth mode with a great selectivity for grain boundaries and step edges. The results of this work can be used for further exploration of the TMD monolayer structure and properties, which is essential for tailoring 2D materials for a specific application in devices.

© 2022 Author(s). All article content, except where otherwise noted, is licensed under a Creative Commons Attribution (CC BY) license (http://creativecommons.org/licenses/by/4.0/). https://doi.org/10.1116/6.0001913

I. INTRODUCTION

Due to their exceptional physical, electrical, and optical characteristics, two-dimensional (2D) transition metal dichalcogenides (TMDs) have generated a lot of attention in the scientific community.[1] Alternative designs for optoelectronic devices are being studied for upcoming technological nodes as Moore's law approaches its scaling limits.[1,2] A new field of study in nanotechnology for 2D materials was established in 2004 by Geim and Novoselov's discovery of a graphene monolayer.[3] Transition metal dichalcogenides (TMDs), which are 2D semiconductors, have shown to be a great substitute for silicon-based transistors in the sub-5 nm range[2,4] owing to their wide range of conductivity measurements. The short-channel effect,[5] which is caused by source-drain tunneling and the loss of gate electrostatic control over the channel, is what prevents silicon-based devices from being further advanced. Whenever the gate length is shortened, a serious on/off current deterioration occurs. Due to their superior semiconductor features, such as high mobility, a wider bandgap, and a lower in-plane dielectric constant, TMD-based transistors perform better than silicon-based transistors.[6–8] However, the thoroughly passivated surface of 2D materials provides the opportunity to create transistors with unparalleled levels of defect-free at the nanoscale range. A low subthreshold swing (70 mV/dec) and a high on/off current ratio (up to 10^8) were two characteristics of the first MoS_2 transistor demonstration.[9] Since TMD monolayer flakes are

© Author(s) 2022

accessible by exfoliation processes, a wide range of TMDs is now being explored in semiconductors.[10,11] Researchers have also made incredible progress in establishing TMD manufacturing methods that are practical for commercial production, such as chemical vapor deposition (CVD). For effective gate control in cutting-edge technology, nanometer-thin high-k dielectric films must be deposited on an ultrathin TMD channel. However, there is currently little knowledge of the processes governing the formation and nucleation of high-k dielectric films during atomic layer deposition (ALD) on TMD materials made by CVD. The majority of reports[12,13] focus on the ALD process settings, the physical characteristics of the generated films, structure determination, and domain size alone. However, TMD CVD's function has not yet been investigated. The majority of CVD-grown TMDs are polycrystalline, and the starting surface as well as the CVD growth conditions have a significant impact on the size, surface coverage, and in-plane orientation of the crystal grains.[14] The subsequent ALD process of high-k dielectric films can be impacted by the TMD grain size, the existence of intragrain defects, surface coverage, and in-plane crystal grain orientation, respectively. Furthermore, selective decoration of the TMD surface structure by ALD can offer a thorough comprehension of the TMD layer structure and characteristics, which is necessary for adjusting the layers to specific applications. We, thus, examine atomic layer deposition (ALD) of Al_2O_3 on CVD-grown TMDs in this study. Self-terminating gas-solid chemical reactions are the foundation of ALD. The ALD deposition principle enables conformal deposition and nanoscale control of layer composition and thickness. ALD has been used successfully in several high-k dielectric applications, as per the reports.[15–19] For instance, ALD has been used to create Si-based dielectric films effectively on FETs with a thickness of less than 2 nm.[12,20,21] Fast layer closure is necessary to create nanometer thin, hole-free dielectric films; hence, the nucleation mechanisms have been addressed.[21,22] When the substrate is not yet entirely covered by the ALD-grown layer, the substrate impacts the growth per cycle (GPC, the quantity of material deposited each reaction cycle) and the growth mode that controls how the material is distributed on the substrate. When the film closes and the GPC (steady growth per cycle) becomes constant, the impact of the original substrate surface fades. Since $HfCl_4$ quickly interacts with the –OH surface groups, the development of HfO_2 layers using $HfCl_4/H_2O$ ALD on a completely hydroxylated SiO_2 surface illustrates rapid film closure.[12] Since $HfCl_4$ is not highly reactive with the H groups of the Si surface, the same mechanism results in sluggish layer closure for an H-terminated Si surface. Another well-known instance of this is the development of Al_2O_3 on H-terminated Si using trimethylaluminum (TMA)/H_2O, which at first develops an island morphology rather than a continuous Al_2O_3 film.[22] As a result, a lot of reactive surface sites are needed for the film to close quickly. TMD materials suspended bond-free surface is an advantage in electrical devices. However, the absence of reactive surfaces makes it difficult to deposit dielectrics via ALD.[23] It has been shown that high dielectric material nucleation on exfoliated TMDs occurs extremely slowly during the ALD process, with the layers not closing until they reach a significant thickness (e.g., >10 nm).[24–29] On the inert surface of TMDs, attempts have been made to resolve the nucleation issue for ALD. These methods, unfortunately, face the risk of oxidizing the TMDs.[30] ALD may enable physisorption-based nucleation by lowering the temperature.[28] Purity is the concern and loses when the ALD temperature is dropped. In addition to this issue, it is unknown how ALD on TMD materials works.[31] Typically, chemisorption mechanisms that occur during the successive, self-limiting surface reactions of ALD precursors are used to explain how ALD grows.[32] However, in addition to chemisorption, extra atomistic interactions, such as physisorption and surface diffusion of adsorbed precursor molecules (species), which are weakly bound, may also contribute to the formation of ALD on 2D materials. Additionally, the creation of nanoparticles from the aggregated species can then disperse and agglomerate.[33–38] In this research, we study the nucleation, development, evolution, and ALD of a polycrystalline monolayer of WS_2 produced via metal-organic CVD. Through complementary physical characterization methods that measure the total quantity of deposited material, its surface coverage, and the Al_2O_3 particle size distribution, the initial nucleation, growth mode, and layer closure processes during ALD are examined (PSD). Assuming selective nucleation at WS_2 grain boundaries, crystal edges, and surface defects, we evaluate the ALD growth process using this model. A lateral growth mechanism is then applied to close the thin films. It is suggested that the theory of NP diffusion and collision effects be used to explain the impact of ALD temperature. Additionally, we investigated the impacts of the early TMA pulses as a functionalization strategy to comprehend their initial nucleation mechanism and their relevance to the ALD process.

II. MATERIALS AND METHODS

A. TMD material preparation and ALD process

To investigate the nucleation and growth mechanisms of Al_2O_3 on a polycrystalline WS_2 monolayer, the ALD Al_2O_3/1.3 Ml WS_2/1.6 μm SiO_2/Si (100) samples were prepared. To stop the development of native oxides, the Si wafers were first cleaned using cyclic HF and then subjected to wet thermal oxidation.[33] Then, using $W(CO)_6$ and H_2S as precursors, a closed WS_2 monolayer was produced by MOCVD at 950 °C, although alternative material sources and surface choices were used and their relevant MOCVD process has been previously reported.[34,35] Al_2O_3 ALD was then created using a Polygon® 8200 platform and a PULSAR® 2000 reactor with an inert gas valve, and the ALD reactor is a 200 °C hot-wall cross-flow reactor type. The temperature was maintained at 18 °C for trimethylaluminum (TMA) and H_2O precursor bubbles. As a carrier gas, nitrogen (N_2) was employed.[35] The samples were shifted into a loading lock before Al_2O_3 ALD was formed to prevent background oxidants' formation.[36]

B. Analysis

AFM is an effective method for characterizing surface morphology. WS_2 surface morphology, grain size distribution, and Al_2O_3 deposition by ALD were all studied using atomic force microscopy (AFM, ICON PT, Brooker, and UHV3500 SPM, RHK) in non-contact mode. By comparing the uncovered WS_2 area to the Al_2O_3 surface area, it can calculate the Al_2O_3 surface coverage and film deterioration as a function of ALD cycles. In this manner, a

30 June 2023 13:30:10

© Author(s) 2022

computer model was used to explore the nucleation and growth process of Al_2O_3 deposition on WS_2 surfaces. The Al_2O_3 surface on the substrate was also examined using a time-of-flight secondary ion mass spectrometer (TOF-SIMS). Based on the secondary ions' depth of escape in a 2D growth mode, the deposited material covers the surface uniformly, and it also intensifies the substrate elements' TOF-SIMS signal (s). A secondary ion's escape depth typically ranges between one and two atomic layers.[37] $I/I_0 = \exp(-t/\lambda)$, where t is the layer thickness and also the secondary ion's escape depth, results in a sharp drop.[38] Since certain areas of the substrate are still exposed after a few cycles in non-2D development, the substrate signal deteriorates significantly and slowly.[39–41] As a result, the substrate signal decay is highly sensitive and may be utilized to track the end and the growth of a film effectively. To determine the vibrations of the WS_2 lattice and a plane in front of the Al_2O_3 ALD, Raman spectra at 523 nm were taken. The elemental abundance of W and S as well as the thickness of the WS_2 film are measured using Rutherford backscattering spectrometry (RBS) with a 1.52 MeV He^+ ion beam.

III. RESULTS AND DISCUSSION

For better interpretation, the information is classified into four sections. We describe the composition and morphology of the polycrystalline WS_2 single crystal layer before ALD in Sec. III A. We trace the growth progress of the Al_2O_3 ALD on the WS_2 single crystal layer up to 600 ALD cycles in Sec. III B. Using AFM, ERD, and TOF-SIMS to examine the surface coverage, morphology, and amount of material deposited (Al areal density), we assess the growth mode and explore the implications of the ALD process settings. We discuss the Al_2O_3 ALD growth mode on polycrystalline WS_2 in Sec. III C. In Sec. III D, we examine how WS_2 crystal domains change in orientation and 2D structure as they develop on single crystals of WS_2.

A. Characterization of WS_2 before ALD

The chemical bonding, surface composition, hydrophilicity, crystal structure, and shape of the 2D material have an impact on the nucleation and growth behavior of ALD on the substrate. To comprehend the structure, crystallinity, and morphology of WS_2 on a SiO_2/Si substrate, we first measured and obtained AFM pictures, RBS data, and Raman spectra. According to Fig. 1(a), the layer is mostly made up of a closed polycrystalline single layer with a few triangular WS_2 crystal grains on top. The SiO_2 substrate is mostly parallel to the basal planes of the WS_2 crystals. According to AFM measurements made after 60 cycles, the closed monolayer's grain size ranges between 10 and 200 nm with an average of 64 nm [Fig. 1(c)]. Triangular grains on the initially closed monolayer have a grain size distribution that ranges from 100 to 1100 nm, with an average of 460 nm [Fig. 1(d)]. A spiral structure with a limited number of layers is generated when a few triangular WS_2 crystals develop. The surface roughness (rms) of WS_2 is 0.4 nm, according to AFM studies.

The elemental amounts of W and S as well as the thickness of the WS_2 layer are determined using Rutherford backscattering spectrometry (RBS). W and S both have a primary content of 1.2×10^{15} and $2.6 \times 10^{15} \pm$ at/cm^2, respectively. The S/W ratio is 2:1, which is almost the stoichiometry predicted for WS_2. The connection that a monolayer of WS_2 consists of 1.0×10^{15} W at/cm^2 assuming the nominal density (7.02 g/cm^3) and ML thickness (0.55 nm) of WS_2 allows the W content measured by RBS to be translated into monolayer content (ML). According to the RBS measurements, 1.3 ML of WS_2 was deposited. Inferring that the MOCVD deposition produces a closed monolayer with a few crystals at the top, we compute the percentage area of triangular crystals in the second layer based on the RBS result, and 30% of the second layer's computed area is made of triangular crystals. The 1.3 ML WS_2 is thought to be composed of a closed WS_2 layer with some sizable triangular crystals in the second layer based on the strong agreement between the AFM and RBS measurements. In other words, as seen in Fig. 1(e), the basal plane of WS_2 crystals in the first (70%) and second (30%) monolayers, step edges, and grain boundaries characterize the WS_2 surface. According to Fig. 1(b), the in-plane (E_{12g}) and out-of-plane (A_{1g}) vibrational modes exhibit vibrations at 355.2 and 417.2 cm^{-1} in the Raman spectrum, respectively.[42] The overall details of the possible models conferred are as follows and their detailed information is included in the following section as well for better understanding. We tried to brief the details as Model 1, Model 2, and Model 3.

Model 1: 2D growth, the ideal ALD growth model, the self-limiting aspect of ALD leads to excellent step coverage and conformal deposition on high aspect ratio structures. Some surface areas will react before other surface areas because of different precursor gas fluxes.

Model 2: Nanoribbon growth, which is the 3D growth model based on the sample surface, in our cases, the major nucleation sites are on the grain boundaries, but all the grain boundaries are highly sensitive and can nuclei on all nucleation site on every cycle, but the noninteractive region will deposit more by the lateral growth.

Model 3: Hemi-cone growth— we found out that even if the grain boundaries are causing selective growth, which leads to the third model, we need to provide the nucleation density value and the growth rate by each cycle number, leading to a slower film closure due to the better quality of the 2D material film surfaces (WS_2).

B. Growth evolution of Al_2O_3 ALD on polycrystalline WS_2

In this section, we discussed Al_2O_3 ALD process development, evolution, and morphology on WS_2. To examine the nucleation and growth processes of Al_2O_3 on WS_2, we utilized a 1.3 ML polycrystalline Al_2O_3 sample and a 1.6 μm SiO_2/Si (100) substrate. After purification with cyclic HF, the influence of native oxide is avoided by thermal oxidation. Trimethylaluminum (TMA) and oxidant H_2O were employed as precursors, bubbling at 18 °C to produce WS_2 films at 950 and 150 °C through the MOCVD process and nitrogen (N_2) was used as a carrier gas. We pumped the chamber up to a 10^{-1} Torr base pressure (P_{base}). The AFM images following Al_2O_3 ALD for various ALD cycles are shown in Figs. 2(a)–2(f). The Al content as estimated by ERD is coupled with the AFM data, Figs. 4(a) and 4(b), from nucleation through linear development, and the evolution of Al_2O_3 and ALD on WS_2

30 June 2023 13:30:10

© Author(s) 2022

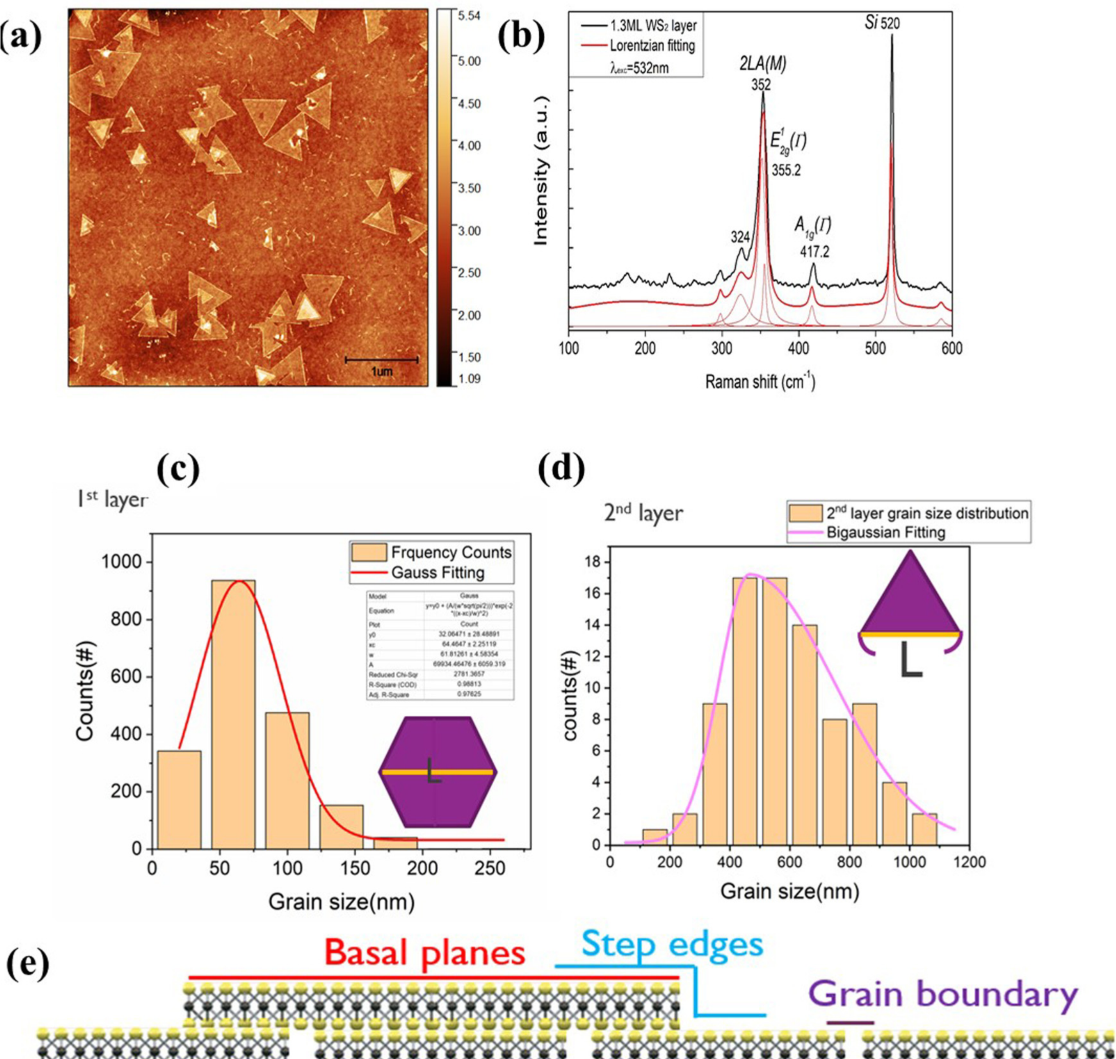

FIG. 1. Chemical state, 2D structure, surface morphology, and continuity investigation of WS_2. (a) AFM image of WS_2 surface in tapping mode. (b) Raman spectra of the as-grown WS_2. (c) AFM analysis of grain size distribution. (d) The grain size distribution of triangular grains sitting on top. (e) The polycrystalline WS_2 film surface was characterized by step edges, grain boundaries, and the basal plane of WS_2 crystals.

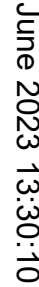
30 June 2023 13:30:10

is investigated. The growth is impeded during the first 400 cycles of Al_2O_3 ALD on WS_2, which is a substantially longer period than Al_2O_3 ALD on H-terminated Si and synthetic MoS_2 produced via sulfurization.[28,38,43] The initial nucleation, the transition state, and the linear growth stage are the three phases that contribute to the general growth mechanism of ALD. WS_2 step edges, grain boundaries, and a few point defects are the only places where Al_2O_3 islands are produced during the first nucleation process, leaving the basal plane mostly uncovered. The nucleation density was calculated based on the surface morphology of the Al_2O_3/WS_2 surface and the number of ALD cycles of the AFM film, as shown in Fig. 4(e). The nucleation density increases nearly linearly throughout the first 200 ALD cycles, suggesting that a rising number of Al_2O_3 nuclei are formed during this period. The initial WS_2 monolayers-enhanced nucleation at the grain boundaries is the primary cause of the growing nucleation density. This increase is influenced by the flushing time after the water pulse, Fig. 4(c), and therefore, it could indicate a slow change in surface composition. The S-H groups at the grain boundaries may slowly oxidize during H_2O pulse and rinsing, which increases the TMA adsorption rate at the grain boundaries, allowing new nuclei to be formed during the first 200 ALD cycles.

© Author(s) 2022

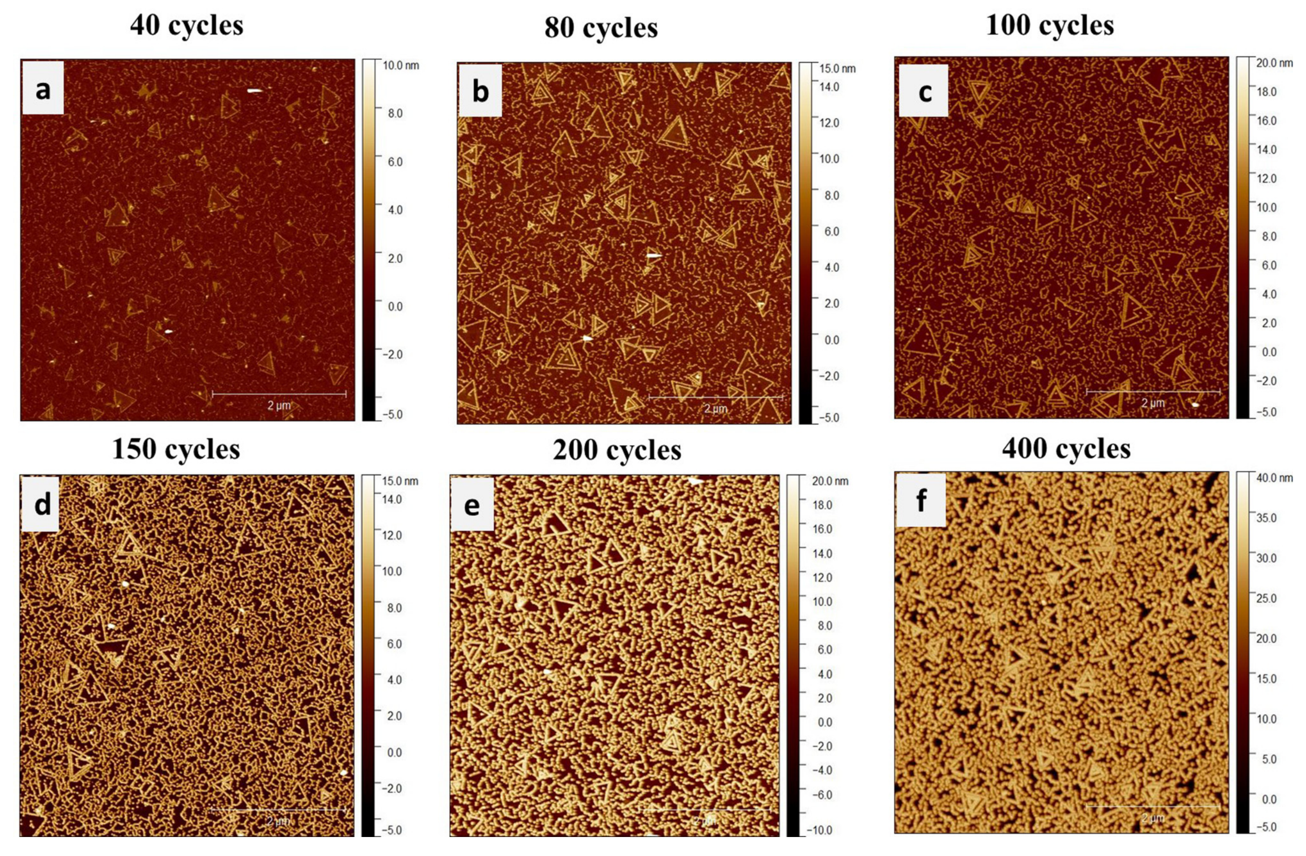

FIG. 2. (a)–(f) AFM image at different cycles of the nucleation growth behaviors of WS_2.

30 June 2023 13:30:10

Despite having a smaller length per area, the density of nuclei generated at the grain boundaries is noticeably higher than the density of nuclei generated at the crystal edges in the first cycle (roughly estimated from the intersection of the linear fit in Fig. 4(e). $\sim 2.1 \times 10^{10}/cm^2$ nuclei in the first cycle ($\sim 0.0078 \times 10^{10}/cm^2$ nuclei per cycle) (there are a smaller number of larger triangular crystals in the second layer compared to a larger number of smaller crystals in the first layer). The AFM images indicate this distinction as well. Due to the closer spacing between the Al_2O_3 nuclei at the crystal borders, continuous nanoribbons form more quickly. The increased nucleation density is consistent with the surface morphology and suggests that there are more surface sites, such as S-H groups, at the crystal edges. There may be a large number of S-H groups on the crystal edges of the triangular WS_2 crystals in the partial second monolayer, which are easily accessible for ligand exchange reactions with TMA and/or H_2O. On the other hand, the first monolayers of WS_2 grains could be partly linked, for instance, by S-bridges. This leads to a lower number, lower accessibility, and lower reactivity of the reactive sites, which is associated with a lower nucleation density and slower coalescence.[42] Finally, the nucleation density reaches a plateau at $3.6 \times 10^{10}/cm^2$ after 200 cycles [Fig. 4(e)]. This may indicate that an equilibrium is reached between adsorption, in which new nuclei are formed, and coalescence of islands, in which their number is reduced.

As a result of conformal Al_2O_3 deposition in both the vertical and horizontal orientations, the nanoribbons eventually coalesce into a nanoscale membrane during the ALD process. In reality, the GPC of Al_2O_3 ALD is not far from the lateral and vertical growth rates of Al_2O_3 nanoribbons developing at the step edges, Fig. 4(c). As a result, between 200 and 600 cycles, the surface coverage gradually rises, and this is the layered closure's limiting factor. After around 600 ALD cycles, linear growth is finally seen, indicating a multilayer closure with 1.65×10^{17} Al atoms/cm^2. In comparison to other substrates, Al_2O_3 ALD at 300 °C requires a substantially higher Al content to accomplish linear growth, such as 1.6×10^{16} atoms/cm^2 or 50 ALD cycles on H-terminated Si and 7.0×10^{16} atoms/cm^2 or 230 ALD cycles on polycrystalline MoS_2 with grain sizes between 10 and 50 nm.[28] After achieving the linear growth condition, the growth cycle (GPC) is 3.2×10^{14} Al atoms/cm^2. In conclusion, the nucleation and growth mechanism are significantly different from the typical 3D key mechanisms proposed in the literature for ALD[44] because of the heterogeneity of the surface and the different adsorption and nucleation kinetics at the grain boundaries and step edges of the WS_2 surface. We infer by

© Author(s) 2022

discussing the outcomes of the ALD processing conditions, such as a lower deposition achieved by reducing the N_2 push flow, which is supported by AFM pictures in Fig. S1.[46] The simulation results for the Hemi-cone model and the 60-cycle model demonstrate strong nucleation, and the push flow has a modest growth rate of less than 150 °C (0.02 nm/cycle). A better film closure is indicated by the observation of points even after the simulation line for 2D development [Figs. 4(a) and 4(b)]. In these analyses, the H_2O solution's rinse duration was adjusted to 10 s to prevent negative impacts on the reaction surface group ([Figs. 4(c) and 4(a)]. The test results of 0–200 cycles are shown, which is at 150 °C temperature, for 80, 100, 150, and 200 cycles. It is clear from the simulation that the 2D growth condition is the same as what we observed from imec clean (Al_2O_3 grows on SiO_2, and the test conditions are the same as the growth of $WS_2/SiO_2/Si$). In contrast, imec clean can simulate 2D growth conditions, such as all growth cycles growing $3.54 \times 10^{15} \times$ growth rate $\times$ cycle number. At low cycle numbers, $WS_2/SiO_2/Si$ can be observed and have low adsorption on the WS_2 surface, which results in particles forming just at step heights, vacancies, and W–S–H bonds. As a result of this, surface irregularities are formed at the initial stage (nonconformal surfaces) because the nucleation density per cycle, growth rate along with grain boundary, as well as geometrical interaction between nanoparticles are accumulated into an F-factor, which is calculated in the second layer closure step: Sum of the growth number per cycle (lateral direction) and proposed hemi-cone model is provided and mentioned in Fig. 3 given below.

In Fig. 4(a), the 0–200 cycle numbers cannot accurately fit the experimental results. This calculation formula will be restricted by the topography of the grain boundary surface if F = 10. Since WS_2 has a limited surface morphology, Fig. 2(a), AFM results show its morphology. This stage covers from the initial stage to the transition stage, so as shown in Fig. 2(e), after all, grain boundaries are covered by Al_2O_3; then, F-factor and nucleation density will no longer be added, only horizontal growth and as shown in Fig. 4(e), nuclei do not increase after 200 cycle number, as in Fig. 4(d). After 200 cycles, the slope of areal density for several ALD cycles gradually becomes a constant value. According to different test conditions, this growth model can determine which one has a faster growth rate. At the same time, it also verifies the WS_2 surface. Under this test condition, a nucleation site is still needed for surface adsorption and growth, Fig. 4(b), and the growth results under different test conditions (low push flow) are obtained. As shown in the AFM results in Fig. S3,[46] it can be seen that the growth still starts from the grain boundary, but the film closure occurs earlier, and the growth from the horizontal direction and the nucleation density has increased significantly, indicating that the horizontal growth rate is much larger than the vertical growth rate, which is the main cause of the faster film closure under the low push flow test condition.

C. Growth mode of Al_2O_3, ALD on polycrystalline WS_2

The ALD develops in various directions on the surface depending on the growth mode, and WS_2 is increased by 60 ALD cycles with some sizable triangular crystals. This is complicated and has to be described appropriately. Instead, the complete layer closure was examined individually by watching the TOF-SIMS W^+ signal decay as a function of Al content and examining the rise in AFM surface coverage as a function of A1 content, Figs. 5(a) and 5(b). Figure 5(a) depicts an Al_2O_3 growth film made from 600 cycles, with a total atom content of $1.65 \times 10^{17}/cm^2$, a thickness of 46 nm, and a WS_2 surface (97% covered). The crystal base surface needs to be shaped into a sizable, inert triangle form. Al_2O_3 in WS_2 experiences a slower membrane closure process, which is consistent with the development in surface resistivity shown on the growth curve, as shown by the less severe decay in Fig. 5(b), compared to the perfect 2D growth. Because of the huge grain size and subsequent stabilization and deception of the signals at TOF-SIMS, which mostly impacts the W^+ signals, the layers are closed by 400–600 ALD processes. When the normalized W^+ signal declines from 10 to 3, it indicates that the layer has completely closed.

The surface coverage and morphological progression from Al_2O_3 to WS_2, Fig. 1(a), can be used to define the growth mode. Early nucleation and growth are driven by thermal ALD self-terminating chemical processes. The borders of the phases and the

30 June 2023 13:30:10

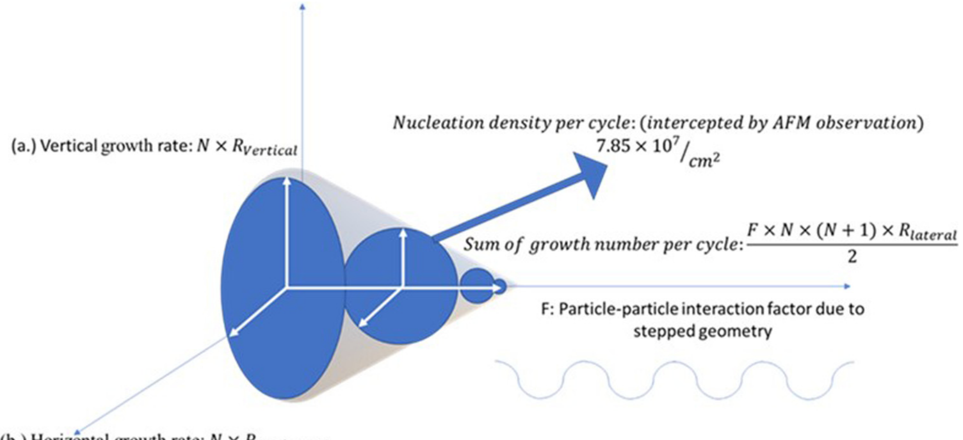

FIG. 3. Hemi-cone model with vertical growth rate (a) and horizontal growth rate (b).

© Author(s) 2022

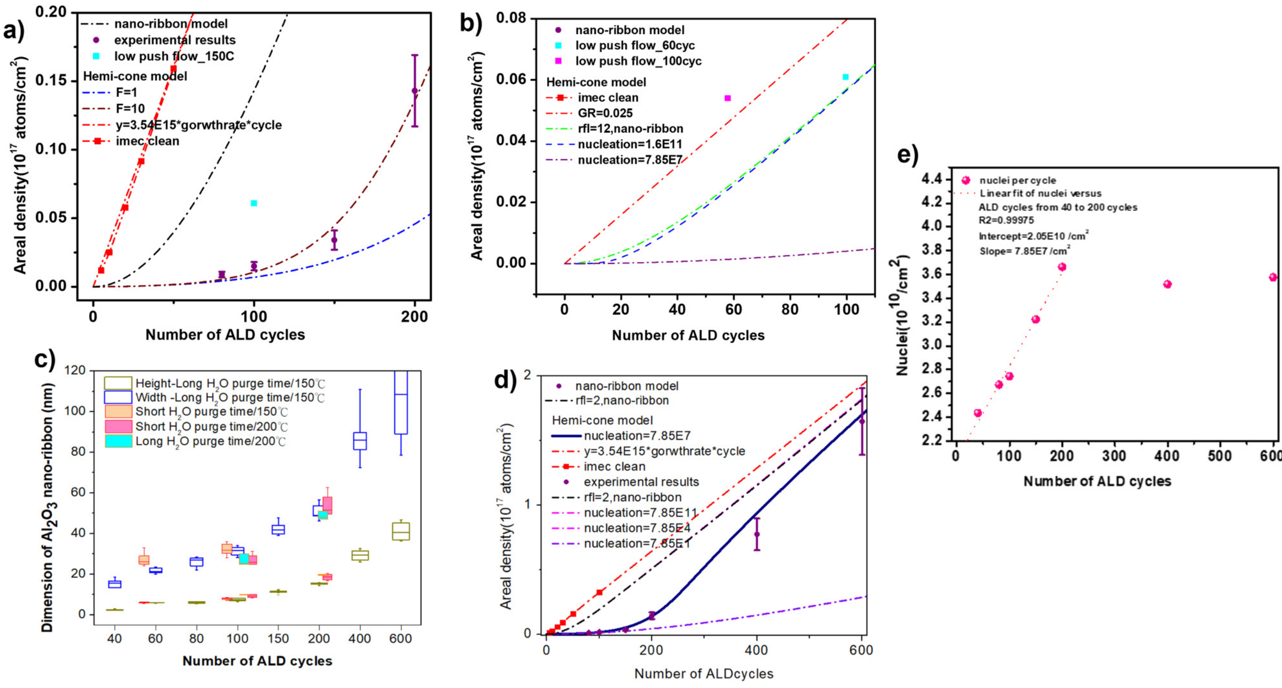

FIG. 4. Growth curve and surface coverage of Al_2O_3 ALD on WS_2. (a) and (b) Al content deposited on WS_2 vs Al_2O_3 ALD cycle number in three different regimes: (i) Initial regime, (ii) transition regime, and (iii) linear growth regime. (The dashed lines are the fitting results based on the proposed growth model.) (c) During purge time of water solution at different ALD cycles. (d) The nucleation density at different ALD cycles. (e) Nucleation growth stages at different ALD cycles.

30 June 2023 13:30:10

grain boundaries are where the majority of the nuclei are deposited. After 40 cycles, Fig. 4(e) displays the ALD reaction outcomes, including the nucleation of crystals along the device's borders. As the ALD reaction proceeds, the grain boundaries increasingly widen until the Al_2O_3 film completely encases the reaction sites at all grain boundaries. The majority of the S–H surface groups at grain boundaries and step edges are covered by transition growth, which causes the nanoparticles to connect and turn into the growth

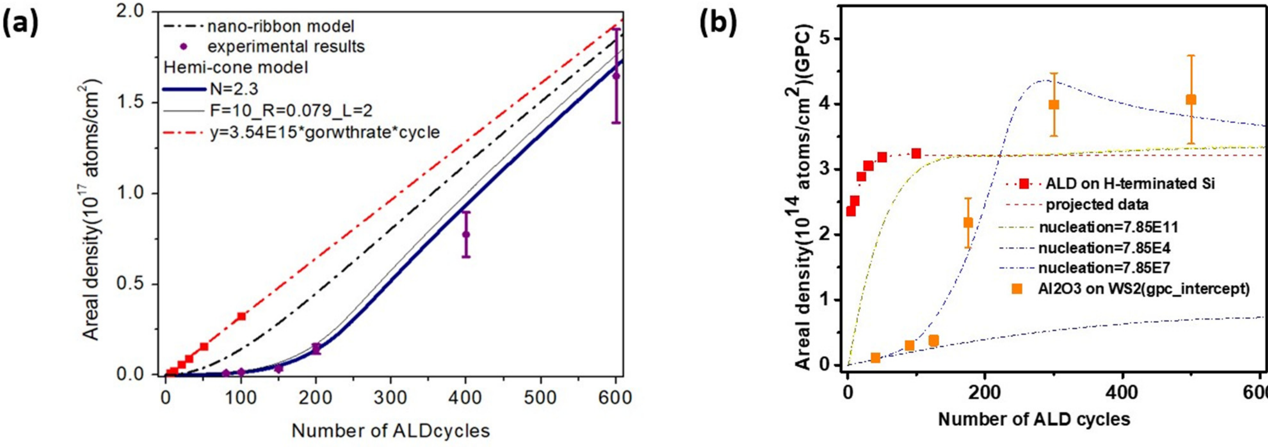

FIG. 5. ALD of Al_2O_3 on polycrystalline WS_2 at different ALD cycles. (a) Lateral and vertical dimensions of Al_2O_3 nanoribbon as a function at different ALD cycle numbers. (b) Growth mode of Al_2O_3, ALD on H-terminated Si.

© Author(s) 2022

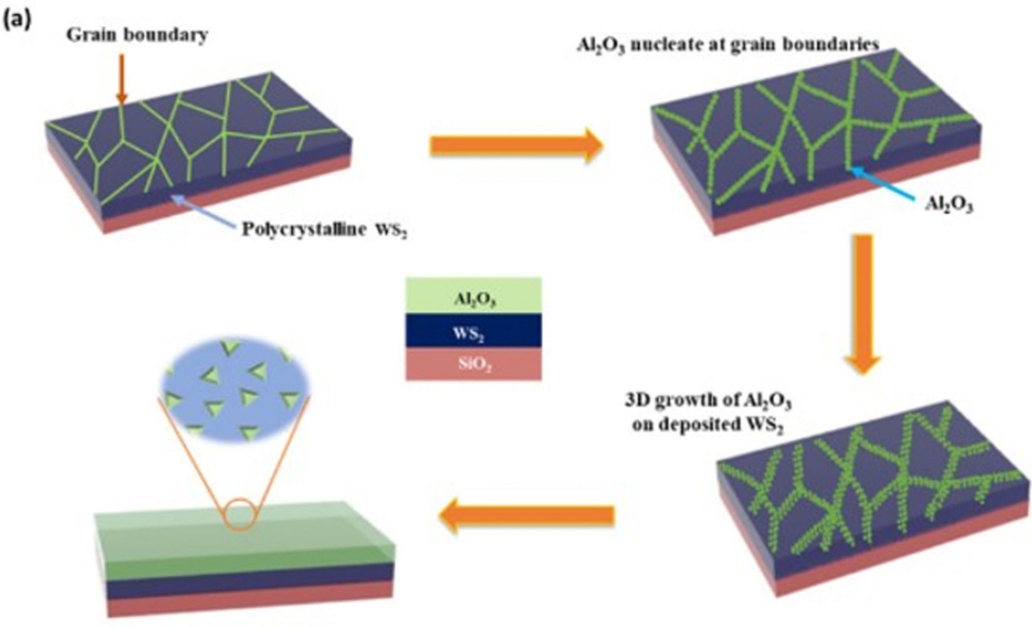

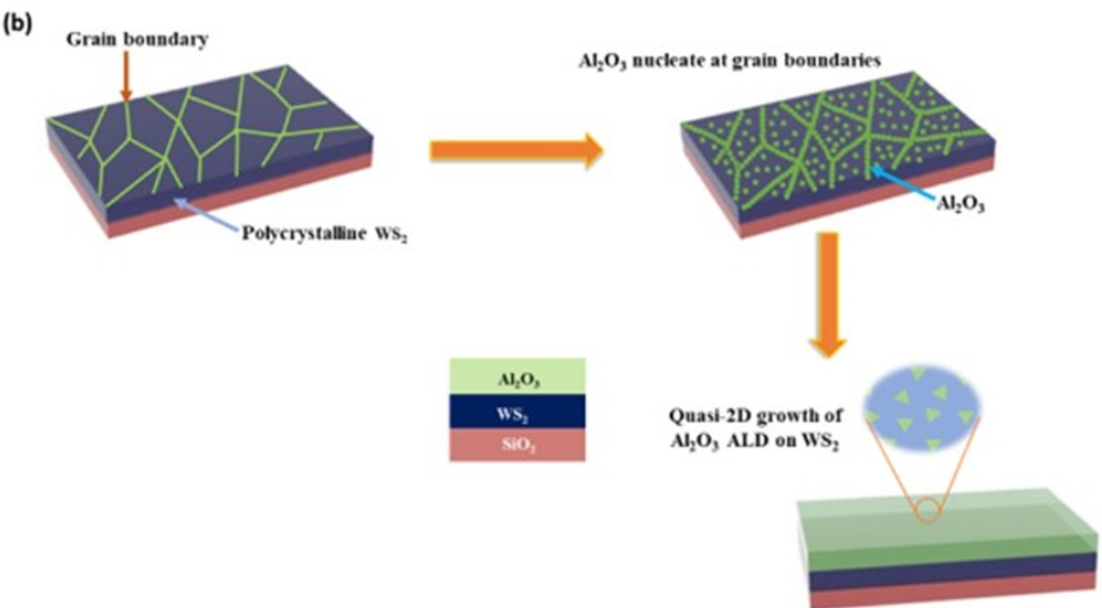

30 June 2023 13:30:10

FIG. 6. Schematic description of the growth model for Al_2O_3 ALD on polycrystalline WS_2. (a) The "ideal" ALD process, in which nuclei form at the step edge and grain boundary of the polycrystalline surface of WS_2, proceeds in 3D. (b) Short purge times result in nucleation on the step edge, grain boundary, and basal plane of WS_2, which allow for a faster layer closure process and a more stable 2D growth mode.

© Author(s) 2022

model of the nanoribbons. The nanoribbons were then stretched both horizontally and vertically. Rapid nucleation happens at the step edge because of the poor coverage of the phase edge, yet this growth mode results in a slowly closing membrane. The WS_2 film oxidizes quickly when exposed to the environment because sulfur is sensitive to air.

D. Growth model for Al_2O_3 ALD on polycrystalline WS_2

The nucleation and growth mechanism for Al_2O_3 ALD on the WS_2 monolayer is complicated, as evidenced by the experimental AFM and ERD data outlined in Sec. III C. Although data show differing adsorption and nucleation kinetics at the grain boundaries and step edges, nucleation mostly occurs at these locations. The nucleation and growth process differ significantly from the typical 3D key mechanisms for ALD that have been suggested in the literature.[43] A more complex nucleation model was created. The extra material contains further information and relationships as in Fig. S2.[46] The growth curves may be statistically evaluated to comprehend the existing model shown in Fig. 6. The computation will be made more straightforward by assuming that the grain boundaries where growth begins are square at the surface. The number of grains per unit area may be computed using the formula $1/l^2$, where l (nm) is the grain size. The total square side length (grain boundary length) is therefore $2/l$ per unit area. Because it is believed to be significantly less than the grain size (∼1 vs 20 nm on average), the width of the grain border is disregarded.[44,45] In agreement with our AFM observations, the lateral and vertical growth rates are assumed to be equal to the GPC of Al_2O_3 ALD, given as Δr. The radius of the Al_2O_3 nanoribbon after n cycles is $r = n \cdot \Delta r$ deposited nanoribbons are modeled as half-cylinders, and the volume after n cycles can be expressed as follows:

$$V = \pi (n \cdot \Delta r)^2 / l. \quad (1)$$

The total Al content (atom density) deposited on WS_2 can be obtained as follows:

$$C = \rho \pi (n \cdot \Delta r)^2 / l, \quad (2)$$

where ρ is the Al atomic density of Al_2O_3 (0.55 nm) calculated based on the density of ALD-Al_2O_3 ($\rho Al_2O_3 = 7.85\, g/cm^3$). In Figs. 6(a) and 6(b), the dashed lines represent the estimated curves (b). The radius of the Al_2O_3 nanoribbon and, therefore, the total surface area of Al_2O_3 grow as the growth in the transition zone advances, which accounts for the rise in GPC. The GPC is even greater before the layer closes than in the linear growth model. Currently, the Al_2O_3 nanoribbon's predicted surface area is more than the surface area of the ideal scenario, which explains why the GPC is higher. Once the WS_2 is completely covered by Al_2O_3 and linear growth is achieved, the appropriate fit of the nonlinear parts of the growth curve shows that the proposed growth model agrees with the experimental results.

IV. CONCLUSIONS

This work provides details and discussion of Al_2O_3 ALD process development, evolution, and morphology on WS_2 including its nucleation and growth processes of Al_2O_3 on WS_2. Large WS_2 crystals have outstanding optical and electrical qualities, as well as great crystal quality, equivalent to samples that have been manually exfoliated and improved their electrical performance with monolayer SiO_2/Si substrates for WS_2 film transistor arrays. We demonstrated that atomic layer deposition of SiO_2/Si on WS_2 TMDs can act as a foundation for optoelectronics, valleytronics, and the next generation of electronic devices. Silicon substrates are subjected to surface modification techniques to reduce their reactivity with ALD reactants and manage silicon oxidation. The creation of such pretreatments will allow for the continuous growth of ALD layers on the substrate of the device that are of varied thicknesses. The growth study findings indicating that the WS_2 basal plane has a modest level of ALD-related inherent reactivity support the idea that functionalizing the TMD surface is necessary to improve the nucleation of ALD. Future studies in this area may benefit from these findings.

ACKNOWLEDGMENTS

This work was financially supported by the "Center for the Semiconductor Technology Research" from The Featured Areas Research Center Program within the framework of the Higher Education Sprout Project by the Ministry of Education (MOE) in Taiwan. Also, it is supported in part by the Ministry of Science and Technology, Taiwan, under Grant Nos. MOST 110-2634-F-009-027 and 110-2622-8-009-018-SB and by the National Chung-Shan Institute of Science and Technology, Taiwan, under No. NCSIST-403-V309(110).

30 June 2023 13:30:10

AUTHOR DECLARATIONS

Conflict of Interest

The authors have no conflicts to disclose.

Author Contributions

Tsu-Ting Lee: Data curation (equal); Formal analysis (equal). **Kashi Chiranjeevulu:** Writing – original draft (equal); Writing – review & editing (equal). **Sireesha Pedaballi:** Software (equal); Writing – review & editing (equal). **Daire cott:** Formal analysis (equal); Resources (equal); Supervision (equal). **Annelies Delabie:** Conceptualization (equal); Resources (equal); Supervision (equal). **Chang-Fu Dee:** Conceptualization (equal); Resources (equal); Software (equal); Supervision (equal). **Edward Yi Chang:** Funding acquisition (equal); Project administration (equal); Resources (equal); Supervision (equal).

DATA AVAILABILITY

The data that support the findings of this study are available within the article and its supplementary material.

REFERENCES

[1] F. Schwierz, Nat. Nanotechnol. **5**, 487 (2010).
[2] G. Zeng and S. Zeng, Comput. Commun. **5**, 39 (2017).
[3] K. S. Novoselov, A. K. Geim, S. V. Morozov, D. Jiang, Y. Zhang, S. V. Dubonos, I. V. Grigorieva, and A. A. Firsov, Science **306**, 666 (2004).
[4] X. Duan, C. Wang, A. Pan, R. Yu, and X. Duan, Chem. Soc. Rev. **44**, 8859 (2015).

© Author(s) 2022

[5]J. Wu, J. Min, and Y. Taur, IEEE Trans. Electron Devices **62**, 3019 (2015).
[6]M. L. Van de Put, M. V. Fischetti, and W. G. Vandenberghe, Comput. Phys. Commun. **244**, 156 (2019).
[7]A. Laturia, M. L. Van de Put, and W. G. Vandenberghe, Npj 2D Mater. Appl. **2**, 6 (2018).
[8]A. Laturia, M. L. Van de Put, and W. G. Vandenberghe, Npj 2D Mater. Appl. **4**, 28 (2020).
[9]A. Nourbakhsh, A. Zubair, S. Joglekar, M. Dresselhaus, and T. Palacios, Nanoscale **9**, 6122 (2017).
[10]Y. Wu *et al.*, Nat. Commun. **6**, 6141 (2015).
[11]W. Choi, N. Choudhary, G. H. Han, J. Park, D. Akinwande, and Y. H. Lee, Mater. Today **20**, 116 (2017).
[12]V. Kranthi Kumar, S. Dhar, T. H. Choudhury, S. A. Shivashankar, and S. Raghavan, Nanoscale **7**, 7802 (2015).
[13]C. Wirtz, T. Hallam, C. P. Cullen, N. C. Berner, M. O'Brien, M. Marcia, A. Hirsch, and G. S. Duesberg, Chem. Commun. **51**, 16553 (2015).
[14]J. You, M. D. Hossain, and Z. Luo, Nano Converg. **5**, 26 (2018).
[15]D. J. Hagen, M. E. Pemble, and M. Karppinen, Appl. Phys. Rev. **6**, 041309 (2019).
[16]X. Meng, J. Mater. Chem. A **5**, 18326 (2017).
[17]R. Gaur, L. Mishra, M. A. Siddiqi, and B. Atakan, RSC Adv. **4**, 33785 (2014).
[18]W. Auwärter, Surf. Sci. Rep. **74**, 1 (2019).
[19]A. Jaggernauth, J. C. Mendes, and R. F. Silva, J. Mater. Chem. C **8**, 13127 (2020).
[20]X. Wang, S. M. Tabakman, and H. Dai, J. Am. Chem. Soc. **130**, 8152 (2008).
[21]H. Kim and P. C. McIntyre, J. Korean Phys. Soc. **48**, 5 (2006).
[22]C.-C. Lin and Y. Kuo, J. Vac. Sci. Technol. B **31**, 030605 (2013).
[23]C. Liu, H. Chen, S. Wang, Q. Liu, Y.-G. Jiang, D. W. Zhang, M. Liu, and P. Zhou, Nat. Nanotechnol. **15**, 545 (2020).
[24]K. M. Price, K. E. Schauble, F. A. McGuire, D. B. Farmer, and A. D. Franklin, ACS Appl. Mater. Interfaces **9**, 23072 (2017).
[25]Y.-S. Lin, I. Kwak, T.-F. Chung, J.-R. Yang, A. C. Kummel, and M.-J. Chen, Appl. Surf. Sci. **492**, 239 (2019).
[26]M. Bosi, RSC Adv. **5**, 75500 (2015).
[27]D. M. Hausmann and R. G. Gordon, J. Cryst. Growth **249**, 251 (2003).
[28]H. Zhang *et al.*, J. Chem. Phys. **146**, 052810 (2017).
[29]T. N. Walter, S. Lee, X. Zhang, M. Chubarov, J. M. Redwing, T. N. Jackson, and S. E. Mohney, Appl. Surf. Sci. **480**, 43 (2019).
[30]E. D. Grayfer, M. N. Kozlova, and V. E. Fedorov, Adv. Colloid Interface Sci. **245**, 40 (2017).
[31]B. Chen *et al.*, ACS Appl. Mater. Interfaces **12**, 42925 (2020).
[32]F. Grillo, H. Van Bui, J. A. Moulijn, M. T. Kreutzer, and J. R. van Ommen, J. Phys. Chem. Lett. **8**, 975 (2017).
[33]Y. Oshima, M. Shandalov, Y. Sun, P. Pianetta, and P. C. McIntyre, Appl. Phys. Lett. **94**, 183102 (2009).
[34]J. O. Williams, Angew. Chem. Int. Ed. Engl. **28**, 1110 (1989).
[35]B. Groven *et al.*, Chem. Mater. **30**, 7648 (2018).
[36]A. Delabie *et al.*, J. Electrochem. Soc. **153**, F180 (2006).
[37]S. M. George, Chem. Rev. **110**, 111 (2010).
[38]M. L. Green *et al.*, J. Appl. Phys. **92**, 7168 (2002).
[39]A. Benninghoven, Angew. Chem. Int. Ed. Engl. **33**, 1023 (1994).
[40]T. Conard, W. Vandervorst, J. Petry, C. Zhao, W. Besling, H. Nohira, and O. Richard, Appl. Surf. Sci. **203–204**, 400 (2003).
[41]A. Delabie *et al.*, J. Appl. Phys. **97**, 064104 (2005).
[42]H. Li, Q. Zhang, C. C. R. Yap, B. K. Tay, T. H. T. Edwin, A. Olivier, and D. Baillargeat, Adv. Funct. Mater. **22**, 1385 (2012).
[43]X. Zhang, X.-F. Qiao, W. Shi, J.-B. Wu, D.-S. Jiang, and P.-H. Tan, Chem. Soc. Rev. **44**, 2757 (2015).
[44]R. L. Puurunen *et al.*, J. Appl. Phys. **96**, 4878 (2004).
[45]G. N. Parsons, J. Vac. Sci. Technol. A **37**, 020911 (2019).
[46]See supplementary material at https://www.scitation.org/doi/suppl/10.1116/6.0001913 for the AFM image of Al_2O_3 ALD on MoS_2, with different testing parameter respect to temperature, N_2 push flow. The hypothesis diagram of the deposition model regarding to the AFM image is also introduced.

30 June 2023 13:30:10

© Author(s) 2022